Time domain reconstruction of sound speed and attenuation in ultrasound computed tomography using full wave inversion

M. Pérez-Liva, J. L. Herraiz, and J. M. UdíasE. MillerB. T. Cox and B. E. Treeby

---

Articles you may be interested in

Angular coherence in ultrasound imaging: Theory and applications
The Journal of the Acoustical Society of America **141**, 1582 (2017); 10.1121/1.4976960

Ultrasonic attenuation and phase velocity of high-density polyethylene pipe material
The Journal of the Acoustical Society of America **141**, 1535 (2017); 10.1121/1.4976689

Multiple-array passive acoustic source localization in shallow water
The Journal of the Acoustical Society of America **141**, 1501 (2017); 10.1121/1.4976214

A point-based scattering model for the incoherent component of the scattered field
The Journal of the Acoustical Society of America **141**, EL210 (2017); 10.1121/1.4976584

Flight parameter estimation using instantaneous frequency and direction of arrival measurements from a single acoustic sensor node
The Journal of the Acoustical Society of America **141**, 1332 (2017); 10.1121/1.4976091

Vibration damping using a spiral acoustic black hole
The Journal of the Acoustical Society of America **141**, 1437 (2017); 10.1121/1.4976687

Time domain reconstruction of sound speed and attenuation in ultrasound computed tomography using full wave inversion[a]

M. Pérez-Liva,[b] J. L. Herraiz, and J. M. Udías
Grupo de Física Nuclear, Dpto. de Física Atómica, Molecular y Nuclear, Universidad Complutense de Madrid, Campus de Excelencia Internacional Moncloa, Avenue Complutense S/N, Facultad de Ciencias Físicas, Madrid 28040, Spain

E. Miller
Department of Electrical and Computer Engineering, Tufts University, 161 College Avenue, Medford, Massachusetts 02155, USA

B. T. Cox and B. E. Treeby
Department of Medical Physics and Biomedical Engineering, University College London, Gower Street, London, WC1E 6BT, United Kingdom

Ultrasound computed tomography (USCT) is a non-invasive imaging technique that provides information about the acoustic properties of soft tissues in the body, such as the speed of sound (SS) and acoustic attenuation (AA). Knowledge of these properties can improve the discrimination between benign and malignant masses, especially in breast cancer studies. Full wave inversion (FWI) methods for image reconstruction in USCT provide the best image quality compared to more approximate methods. Using FWI, the SS is usually recovered in the time domain, and the AA is usually recovered in the frequency domain. Nevertheless, as both properties can be obtained from the same data, it is desirable to have a common framework to reconstruct both distributions. In this work, an algorithm is proposed to reconstruct both the SS and AA distributions using a time domain FWI methodology based on the fractional Laplacian wave equation, an adjoint field formulation, and a gradient-descent method. The optimization code employs a Compute Unified Device Architecture version of the software *k*-Wave, which provides high computational efficiency. The performance of the method was evaluated using simulated noisy data from numerical breast phantoms. Errors were less than 0.5% in the recovered SS and 10% in the AA. © *2017 Acoustical Society of America*.
[http://dx.doi.org/10.1121/1.4976688]

I. INTRODUCTION

Ultrasound computed tomography (USCT) is a non-invasive radiation-free medical imaging technique with promising capabilities to resolve soft tissue structures in the body. In this technique, the tissue is imaged using a set of ultrasound transducers that are located surrounding a region of interest (Ruiter *et al.*, 2012; Medina-Valdés *et al.*, 2015). Each of the transducers acts as the source of an ultrasound field in turn, while the rest of the transducers record the temporal ultrasound signals that carry information about the different structures encountered during propagation. The complete data set is used to recover the spatial distribution of acoustic properties within the region of interest. Many geometrical configurations for the transducer locations have been investigated (Johnson *et al.*, 2007; Duric *et al.*, 2015; Kretzek *et al.*, 2015). A common arrangement consists of a ring of transducers that can be vertically displaced along its central axis to scan the whole breast plane by plane. This configuration ensures that both scattered and direct waves are detected within each two-dimensional (2D) imaging plane.

The acoustical property most studied with transmission USCT is the speed of sound (SS), as it is well correlated with the density of the material (Mast, 2000). Therefore, its use has been proposed for breast cancer detection (Duric *et al.*, 2008; Li *et al.*, 2008a,b; Simonetti *et al.*, 2009; Boyd *et al.*, 2010; Li *et al.*, 2014; Duric *et al.*, 2015) as it may yield images with similar contrast and, therefore, analogous structural information to images obtained from x-ray mammograms. As a result, imaging the SS could provide a useful alternative to detect breast cancer with relatively low-cost setups, avoiding the radiation dose and painful breast compression required in x-ray mammography. On the other hand, acoustic attenuation (AA) can provide enhanced contrast for different tissue types compared to SS (Mast, 2000). AA varies more with tissue type than density or SS, so it may improve significantly the detectability of masses in the breast. The combination of both SS and AA images may also allow better discrimination between benign and malignant masses (Duric *et al.*, 2009; André *et al.*, 2013).

Several methods have been proposed to reconstruct transmitted USCT data (Devaney, 1981, 1982; Wiskin *et al.*,

---

2007; Li *et al.*, 2009; Roy *et al.*, 2010; Simonetti *et al.*, 2009; Perez-Liva *et al.*, 2015; Wang *et al.*, 2015). Approximate models, such as the Born or Rytov linearization or ray-tracing algorithms that employ the principles of geometrical optics are usually used (Devaney, 1981, 1982; Li *et al.*, 2009). Codes based on approximate models typically exhibit fast convergence but limited spatial resolution, which is an important limitation for breast imaging considering the dimensions of the breast and the size of the lesions that must be detected. Alternatively, algorithms that directly solve the wave equation, also known as full wave inversion (FWI) methods, have shown the best results in terms of detectability, resolution, and artifact control (Wiskin *et al.*, 2007; Roy *et al.*, 2010; Anis *et al.*, 2014; Li *et al.*, 2014; Wang *et al.*, 2015). These methods have been mostly adapted from the geophysical techniques of waveform tomography (Tarantola, 1987; Song *et al.*, 1995; Pratt *et al.*, 2007). FWI not only facilitates the detection of very small masses, but also provides additional details of the shape and margins of the structures of the breast, which could play a role in the discrimination between benign and malignant structures (Fornage *et al.*, 1989). The use of FWI has been limited due to its computational burden, as it involves solving a large-scale ill-posed non-linear optimization problem. Fortunately, the significant acceleration provided by parallel processing with graphics processing units (GPUs) has allowed a considerable reduction in execution times. Combined with the use of optimized numerical methods to solve the wave equation (Treeby and Cox, 2010a; Treeby *et al.*, 2012; Treeby and Cox, 2014), the efficiency of image reconstruction using FWI can be significantly improved.

Currently, the FWI methods used to reconstruct the SS and the AA are quite different. The reconstruction of SS (Wiskin *et al.*, 2007; Roy *et al.*, 2010; Anis *et al.*, 2014; Wang *et al.*, 2015) is generally performed in the time domain neglecting the presence of AA. In contrast, the reconstruction of AA using FWI, despite being extensively studied in seismology (Tarantola, 1987; Song *et al.*, 1995; Pratt *et al.*, 2007), has been far less studied in the context of USCT. In previous works (Pratt *et al.*, 2007; Li *et al.*, 2014; Sandhu *et al.*, 2016), a frequency domain FWI formulation for USCT was introduced to obtain the quality factors of the tissues (which indicates the energy loss per cycle) to characterize the AA. The method employs a combination of several carefully chosen fixed-frequencies (working from long to short wavelengths), which requires the solution of several minimization problems and increases the computational cost of the inversion process. Moreover, the mean-squared cost function generally employed in FWI often exhibits a large number of local minima, particularly at high frequencies. Fixed-frequency algorithms are vulnerable to getting stuck on erroneous solutions (Mast, 1999; Lin *et al.*, 2000). This calls for the use of time-domain methods where the entire bandwidth of the signals can be employed during reconstruction (Lin *et al.*, 2000). As SS and AA can be obtained from the same transmitted data, it is desirable to have a common reconstruction framework capable of exploiting, in a computationally efficient manner, the image-quality advantages provided by FWI methods. In this work, a FWI strategy for USCT to recover both the SS and AA distributions in the time domain is proposed.

The remainder of the paper is structured as follows. First, in Sec. II, the problem is introduced, including a description of the acoustic forward model, the optimization approach used to reconstruct the acoustic parameters of interest, and the derivation of the expressions for the functional gradients used in the optimization. In Sec. III, the main features of the optimization code are described. In Sec. IV, the performance of the proposed method is tested with two cases of simulated data: an ideal case of noiseless data with a simple numerical phantom and a realistic numerical breast phantom using noisy data. Section V contains a discussion and summary.

II. ALGORITHM FORMULATION

A. Notation and forward model

Consider a lossy medium in which the acoustic absorption follows a frequency power law of the form

$$\alpha = \alpha_0 \omega^y, \tag{1}$$

where α_0 is the absorption proportionality coefficient in Np (rad/s)$^{-y}$ m^{-1}, ω is the temporal frequency in rad/s, and y is the power law exponent [for the current work, this is assumed to be constant and equal to 1.5, the value given for breast tissue in Duck (1990)]. The linear propagation of acoustic waves in this medium can be described by the fractional Laplacian wave equation (Chen and Holm, 2004; Treeby and Cox, 2010b; Treeby *et al.*, 2012)

$$\Box_\alpha^2 p(\boldsymbol{r}, t) = S(\boldsymbol{r}, t). \tag{2}$$

Here $p(\boldsymbol{r}, t)$ is the acoustic pressure as a function of spatial position $\boldsymbol{r}$ and time t, S is a source term, and $\Box_\alpha^2$ denotes the lossy D'Alembertian operator

$$\Box_\alpha^2 \equiv \frac{1}{c^2} \frac{\partial^2}{\partial t^2} - \nabla^2 - \tau_1 (-\nabla^2)^{y/2} \frac{\partial}{\partial t} - \tau_2 (-\nabla^2)^{(y+1)/2}, \tag{3}$$

where c is the SS. The final two terms in Eq. (3) account for acoustic absorption and dispersion, where τ_1 and τ_2 are given by

$$\tau_1 = -2\alpha_0 c^{y-1}, \quad \tau_2 = 2\alpha_0 c^y \tan\left(\frac{\pi y}{2}\right). \tag{4}$$

In the preceding equations, c and α_0 may vary as a function of spatial position $\boldsymbol{r}$.

B. Inverse problem

The task in USCT is to recover the spatial distribution of the acoustic medium properties using experimental measurements recorded by an array of ultrasound transducers, where each transducer acts as the source in turn. Here, the SS and AA distributions, given by the functions $c(\boldsymbol{r})$ and $\alpha_0(\boldsymbol{r})$, respectively, are obtained using an iterative process.

This process minimizes the global norm of the deviations between the experimental pressure field measured at the receiver positions p^{obs} and the signals p at the same locations simulated using a numerical model

$$\varepsilon = \frac{1}{2}\sum_{m=1}^{M}\int_0^T \left[p(\boldsymbol{r}_m,t) - p^{\text{obs}}(\boldsymbol{r}_m,t)\right]^2 dt + \mu R_{\text{TV}}. \quad (5)$$

Given a ring array comprised of N detectors, here, m represents each of the $M = N(N-1)$ pairs of emitter-receiver transducers of the tomographic ultrasound setup, $\boldsymbol{r}_m$ defines the positions of the receiving transducers, T is the length of the time window employed to record the signals, μ is a regularization parameter, and R_{TV} is a regularization function that aims to encode *a priori* information about the actual solution.

FWI is typically ill-posed, its solution is not unique, and the property maps may not be reconstructed stably because of insufficient data being available and because the data are affected by noise (Jackson, 1972). Consequently, regularization is required in order to get a unique and stable solution and to eliminate artifacts due to noise. Here, an edge-preserving regularization method based on total variation (TV) is used (Rudin *et al.*, 1992). This avoids over-smoothing and acts to preserve the edge information of the reconstructed images. The TV regularization term can be written as

$$R_{\text{TV}} = \sum_{i,j}\sqrt{\xi_{x,i,j}^2 + \xi_{y,i,j}^2 + \theta}, \quad (6)$$

where $\xi_{x,i,j}$ and $\xi_{y,i,j}$ are the derivatives of the acoustical property ξ with respect to x and y, respectively, at the pixel (i,j). The parameter θ ensures that R_{TV} is continuously differentiable.

To perform the minimization, the functional gradient of the cost function defined in Eq. (5) with respect to the acoustic property being recovered (i.e., the Frechet derivative) is employed. This provides the direction in the vector space of the unknowns in which the distribution must be modified at each iterative step of the reconstruction algorithm to minimize the error (Norton, 1999). However, the cost function given in Eq. (5) is affected by both c and α_0 distributions. To reduce the complexity of solving the optimization problem over both distributions simultaneously, an alternating minimization algorithm is used (Niesen *et al.*, 2009). In this technique, the optimization problem is divided into two subproblems, one in which c is estimated for a fixed α_0 and another in which α_0 is estimated for a fixed c. Once the expressions for the functional gradient are known for both distributions of interest independently, i.e., $\partial\varepsilon/\partial c$ to update the SS using a fixed AA map, and $\partial\varepsilon/\partial\alpha_0$ to update the AA map based on a fixed SS map, they can be used in a gradient-based minimization algorithm. Here, the method of steepest descent is used, where the update equations for the SS and AA are given by

$$c^{n+1}(\boldsymbol{r}) = c^n(\boldsymbol{r}) + \lambda_c{}^n\frac{\partial\varepsilon^n}{\partial c}, \quad (7)$$

$$\alpha_0{}^{n+1}(\boldsymbol{r}) = \alpha_0{}^n(\boldsymbol{r}) + \lambda_{\alpha_0}{}^n\frac{\partial\varepsilon^n}{\partial\alpha_0}. \quad (8)$$

Here, λ^n is the step size for the nth iteration, which is calculated using a line-search method (Snyman, 2005).

C. Functional gradient to update the sound speed distribution

The derivative of the error functional ε with respect to the SS (i.e., the functional gradient) can be found from Eq. (5),

$$\frac{\partial\varepsilon}{\partial c} = \sum_{m=1}^{M}\int_0^T\left[p(\boldsymbol{r}_m,t) - p^{\text{obs}}(\boldsymbol{r}_m,t)\right]\frac{\partial p(\boldsymbol{r}_m,t)}{\partial c}\,dt$$
$$+ \mu\nabla R_{\text{TV}}, \quad (9)$$

where ∇R_{TV} is the gradient of the regularization function R_{TV}, which can be calculated numerically (Peyré, 2009). An efficient way to calculate the functional gradient given by Eq. (9) can be found using the adjoint approach (Norton, 1999). First, an equation for the derivative inside the integral (the Jacobian) can be found by considering that a perturbation to the SS, Δc, at a point $\boldsymbol{r}_p$ will cause a small change $\Delta p(\boldsymbol{r},t)$ in the pressure field. Noting that $(x + \Delta x)^a \approx x^a + ax^{a-1}\Delta x$, a perturbed version of Eq. (2) can be written as

$$\left\{\left(\frac{1}{c^2} - \frac{2\Delta c\delta(\boldsymbol{r}-\boldsymbol{r}_p)}{c^3}\right)\frac{\partial^2}{\partial t^2} - \nabla^2\right.$$
$$+ 2\left(c^{y-1} + (y-1)c^{y-2}\Delta c\delta(\boldsymbol{r}-\boldsymbol{r}_p)\right)\alpha_o(-\nabla^2)^{y/2}\frac{\partial}{\partial t}$$
$$\left.- 2\left(c^y + yc^{y-1}\Delta c\delta(\boldsymbol{r}-\boldsymbol{r}_p)\right)\alpha_o\tan\left(\frac{\pi y}{2}\right)(-\nabla^2)^{(y+1)/2}\right\}$$
$$\times (p + \Delta p) = S. \quad (10)$$

Using Eq. (2), discarding small terms, and dividing by Δc suggests the following equation for the dependence of the pressure field on the SS:

$$\Box_\alpha^2\frac{\partial p}{\partial c} = \left\{\left(\frac{2}{c^3}\delta(\boldsymbol{r}-\boldsymbol{r}_p)\right)\frac{\partial^2}{\partial t^2}\right.$$
$$- 2(y-1)c^{y-2}\delta(\boldsymbol{r}-\boldsymbol{r}_p)\alpha_o(-\nabla^2)^{y/2}\frac{\partial}{\partial t}$$
$$\left.+ 2yc^{y-1}\delta(\boldsymbol{r}-\boldsymbol{r}_p)\alpha_o\tan\left(\frac{\pi y}{2}\right)(-\nabla^2)^{(y+1)/2}\right\}p. \quad (11)$$

The corresponding adjoint wave equation can be defined as (Norton, 1999)

$$\Box_\alpha^2 p^*(\boldsymbol{r},T-t) = \sum_{m=1}^{M}\left[p(\boldsymbol{r}_m,t) - p^{\text{obs}}(\boldsymbol{r}_m,t)\right]\delta(\boldsymbol{r}-\boldsymbol{r}_m). \quad (12)$$

Note, practically this can be implemented by defining the adjoint source term as the time-reversed difference between simulated $p(\boldsymbol{r}_m,t)$ and measured $p^{\text{obs}}(\boldsymbol{r}_m,t)$ data through a

change of variables $t \rightarrow T - t$, solving for the adjoint field $p^*(\boldsymbol{r}, t)$ and then again reversing in time to give $p^*(\boldsymbol{r}, T - t)$. Alternatively, the wave model could be run backward in time.

Next, multiplying Eq. (11) by $p^*(r, T - t)$ and Eq. (12) by $\partial p / \partial c$, subtracting the resulting two expressions and then integrating over time and space gives

$$\frac{\partial \varepsilon}{\partial c(\boldsymbol{r}_p)} = \int_0^T p^*(\boldsymbol{r}_p, T - t)(\Gamma_1 + \Gamma_2 + \Gamma_3) p(\boldsymbol{r}_p, t)\, dt + \Gamma_4,$$

$$\Gamma_1 = \frac{2}{c^3} \frac{\partial^2}{\partial t^2}, \quad \Gamma_2 = -2\alpha_0(y-1)c^{y-2}(-\nabla^2)^{y/2} \frac{\partial}{\partial t},$$

$$\Gamma_3 = 2\alpha_0 y c^{y-1} \tan\left(\frac{\pi y}{2}\right)(-\nabla^2)^{(y+1)/2}, \quad \Gamma_4 = \mu \nabla R_{\mathrm{TV}},$$

(13)

where we have used Eq. (9) and the fact that $\iint \{p^* \Box_\alpha^2 (\partial p / \partial c) - (\partial p / \partial c) \Box_\alpha^2 p^*\}\, dt\, dV = 0$. As the point of the perturbation $\boldsymbol{r}_p$ is arbitrary, Eq. (13) holds for any $\boldsymbol{r}$.

When the relative contributions of the terms $\Gamma_1 p$, $\Gamma_2 p$, and $\Gamma_3 p$ in Eq. (13) to the overall solution is analyzed numerically (using typical SS and AA values for several soft tissues), it can be seen that the terms Γ_2 and Γ_3 are several orders of magnitude smaller than Γ_1. Consequently, these terms can be neglected from the expression of the functional gradient in order to simplify and speed up the calculations. The resulting approximate expression for the gradient is therefore

$$\frac{\partial \varepsilon}{\partial c} \approx \int_0^T \frac{2}{c^3} \left(\frac{\partial^2 p}{\partial t^2}\right) p^*(T - t)\, dt + \mu \nabla R_{\mathrm{TV}},$$

(14)

which coincides with previous works for the lossless medium approximation (Zhou *et al.*, 1995; Wang *et al.*, 2015).

D. Functional gradient to update the attenuation distribution

Following the same methodology in Sec. II C, the functional gradient with respect to the absorption coefficient is given by

$$\frac{\partial \varepsilon}{\partial \alpha_0} = \sum_{m=1}^{M} \int_0^T \left[p(\boldsymbol{r}_m, t) - p^{\mathrm{obs}}(\boldsymbol{r}_m, t) \right] \frac{\partial p(\boldsymbol{r}_m, t)}{\partial \alpha_0}\, dt$$
$$+ \mu \nabla R_{\mathrm{TV}}.$$

(15)

A small change in the absorption coefficient $\Delta \alpha_o$ at point $\boldsymbol{r}_p$ will result in a small change in the pressure field Δp. The perturbed wave equation can be written as

$$\left\{ \frac{1}{c^2} \frac{\partial^2}{\partial t^2} - \nabla^2 + 2c^{y-1}(\alpha_o + \Delta \alpha_o \delta(\boldsymbol{r} - \boldsymbol{r}_p))(-\nabla^2)^{y/2} \frac{\partial}{\partial t} \right.$$
$$\left. - 2c^y(\alpha_o + \Delta \alpha_o \delta(\boldsymbol{r} - \boldsymbol{r}_p)) \tan\left(\frac{\pi y}{2}\right)(-\nabla^2)^{(y+1)/2} \right\}$$
$$\times (p + \Delta p) = S.$$

(16)

Discarding small terms and using Eq. (2) yields

$$\Box_\alpha^2 \frac{\partial p}{\partial \alpha_o} = -2c^{y-1}\delta(\boldsymbol{r} - \boldsymbol{r}_p)(-\nabla^2)^{y/2} \frac{\partial p}{\partial t}$$
$$+ 2c^y \delta(\boldsymbol{r} - \boldsymbol{r}_p) \tan\left(\frac{\pi y}{2}\right)(-\nabla^2)^{(y+1)/2} p.$$

(17)

As above, multiplying Eq. (17) by $p^*(T - t)$ and Eq. (12) by $\partial p / \partial \alpha_0$, subtracting the resulting two expressions, and then integrating over time and space gives an expression for the functional gradient in terms of the forward and adjoint fields

$$\frac{\partial \varepsilon}{\partial \alpha_0} = \int_0^T p^*(\boldsymbol{r}, T - t) \left(-2c^{y-1}(-\nabla^2)^{y/2} \frac{\partial}{\partial t} \right.$$
$$\left. + 2c^y \tan\left(\frac{\pi y}{2}\right)(-\nabla^2)^{(y+1)/2} \right) p(\boldsymbol{r}, t)\, dt + \mu \nabla R_{\mathrm{TV}}.$$

(18)

Here we have used Eq. (15) and the fact that $\iint \{p^* \Box_\alpha^2 (\partial p / \partial \alpha_0) - (\partial p / \partial \alpha_0) \Box_\alpha^2 p^*\}\, dt\, dV = 0$. Note that the fractional Laplacian term in Eq. (18) becomes simpler to compute in the Fourier domain (Chen and Holm, 2004; Treeby and Cox, 2010b)

$$(-\nabla^2)^y p(r, t) = \mathcal{F}^{-1}\{k^{2y} \mathcal{F}[p(r, t)]\},$$

(19)

where $\mathcal{F}$ and $\mathcal{F}^{-1}$ are the forward and inverse Fourier transforms, respectively, and k is the wave number matrix.

III. ALGORITHM IMPLEMENTATION

A. Numerical implementation

In this work, the fractional Laplacian wave equation given in Eq. (2), used for forward and backward propagation of the pressure field, is solved using a parallelized GPU version of the open-source k-Wave toolbox written in c++ and Compute Unified Device Architecture (CUDA) (Treeby and Cox, 2010a; Treeby *et al.*, 2012). This uses the k-space pseudospectral method to discretize the governing equations, which allows accurate simulations close to the Nyquist limit of two grid points per minimum wavelength. Compared to conventional finite-difference methods, this significantly reduces the size of the computational grid and, consequently, the memory and execution time needed for realistic domain sizes. In order to facilitate integration with the CUDA version of k-Wave, the entire optimization algorithm was implemented in c++.

B. Comparison with finite difference estimations

In order to verify the expressions obtained in Secs. II C and II D for the functional gradients, they were compared to functional gradients calculated using a computationally expensive finite difference approximation. The SS distribution was perturbed at each point in turn along a given line by a small amount Δc, and the change in the error functional $\Delta \varepsilon$ was recorded. In this way a finite difference gradient can be
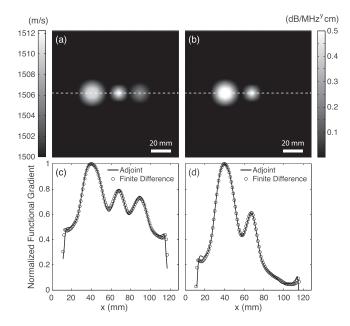
FIG. 1. Comparison between the functional gradients obtained using finite differences and the adjoint method. (a) SS distribution employed for the simulations. (b) AA distribution. (c) Comparison of functional gradients for the SS. The gradient is taken through the SS map at the position shown with the white dashed line. (d) Comparison of functional gradients for the acoustic absorption.
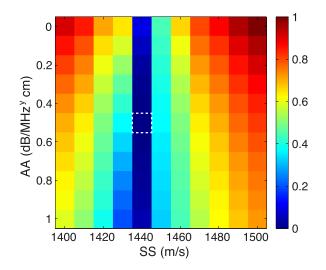

FIG. 2. (Color online) Example of the global error behavior (normalized to the maximum value) around the actual SS and AA values for a homogeneous distribution of acoustic material properties. The intersection of the true values (which corresponds to the global minimum) is shown with the white dashed square.

computed as $\Delta\varepsilon/\Delta c$. This process was repeated in the same way for the AA distribution to obtain the finite difference gradient $\Delta\varepsilon/\Delta\alpha_o$. For both tests, the SS and the AA distributions shown in Figs. 1(a) and 1(b) were used. A circular array of 200 transducers with a diameter of 128 mm and a central frequency of 1 MHz was employed for the simulations using k-Wave. Both distributions were perturbed along the line $y = 64$ mm. Figures 1(c) and 1(d) show the comparison between the finite difference functional gradients and those obtained using the adjoint method [Eqs. (14) and (18)]. Both methods give similar gradients, verifying that the adjoint method was formulated and implemented correctly.

C. Order for the alternating minimization method

As described in Sec. II B, we propose to reconstruct the SS and AA maps using an alternating minimization method. In order to optimize both distributions independently, it is important to follow a certain order in the optimization process. This can be illustrated with a simple numerical example. Consider the recovery of SS and AA maps in a homogeneous medium with $c = 1440$ m/s and $\alpha_0 = 0.5$ dB/[MHz^y cm] using a ring array with radius 54 mm and $N = 200$ uniformly distributed transducers. Using a single emitter, the global error resulting from testing a range of values of SS (1400–1500 m/s) and AA (0–1 dB/[MHz^y cm]) can be calculated using Eq. (5). As noise is not included in this example, the term μ in Eq. (5) can be set to zero. Due to the symmetry of the problem, it is not necessary to extend the calculations to all 200 emitters. The resulting error distribution is given in Fig. 2. The SS optimization has a relatively small dependence on the initial AA map. For the range of AA values tested, it is possible to reach the minimum of the global error with respect to the SS

distribution, regardless of the initial AA map. This is also evident in Eq. (14), which shows that the update of the SS distribution is independent on the AA distribution. By contrast, the optimal reconstruction of AA strongly depends on the accuracy of the SS map. It is necessary to be close to the actual SS map to converge to the correct AA distribution. Moreover, as Eq. (18) contains an explicit dependence on the SS distribution, small deviations in the SS distribution from the true values may propagate and create significant artifacts in the reconstructed α_0 distribution. Therefore, in the reconstruction of AA, it is important to use a SS distribution as close as possible to the actual one. Consequently, in order to minimize both distributions, a reasonable approach is to first solve for the SS distribution with an initial estimation of the AA, and then employ this SS distribution to recover the actual AA distribution.

D. Ordered subsets method

The functional gradients given in Eqs. (14) and (18) require running the computational model to solve the wave equation twice per iteration: once for the forward propagation of the pressure field generated by the emitter to obtain p, and a second time for the backward propagation to obtain the adjoint field p^*. This operation has to be performed sequentially for each emitter in each iteration. This means that the total number of times the wave equation needs to be solved per iteration is twice the number of transducers (to obtain p and p^*), plus the number of evaluations the line-search algorithm may need. In many tomographic reconstruction problems with a high level of computational burden, the ordered-subsets method has been used to improve the tractability of calculations without significantly compromising image quality (Hudson and Larkin, 1994). This approach consists of splitting the data into subsets which each contain a fraction of the total number of projections (here a *projection* is understood as the data recorded for all the receivers connected with a single emitter). The

functional gradients are computed for each projection of the set but instead of using the global error functional as defined in Eq. (5) for all the possible emitter-receiver pairs, an approximation to the error functional is used instead for each subset. This is defined as the difference between the observed and the estimated signals for the subset M' of emitters and receiver pairs m' for the subset s,

$$\varepsilon^s \approx \frac{1}{2} \sum_{m'=1}^{M'} \int_0^T \left[p(\boldsymbol{r}_{m'}, t) - p^{\mathrm{obs}}(\boldsymbol{r}_{m'}, t) \right]^2 dt + \mu R_{\mathrm{TV}}.$$

(20)

The functional gradients of the error are calculated using similar expressions to Eqs. (14) and (18) but in this case, the fields p^* and p are computed only with those emitter and receiver pairs included in the given subset. The same process is repeated for all subsets to complete a full iteration. This way, the entire data set from all the emitter-detector pairs are employed in a full iteration, but the estimation of the image is updated several times per iteration, speeding up convergence.

E. Initial sound speed and attenuation estimates

As an initial estimate of the SS and AA distributions, a reconstruction based on filtered back projection (FBP) was employed. This is based on a high-frequency approximation of the wave equation, which neglects the refraction experienced when passing through media with different SS, i.e., the propagation of waves is described by straight lines connecting emitter and receiver pairs. FBP can provide a very fast first estimation of the acoustical properties under study ($\sim$0.3 s for the cases studied in Sec. IV). To obtain the FBP-SS image, the first arrival or time-of-flight values of the signals between the emitters and the receivers were calculated (Perez-Liva *et al.*, 2015). These time-of-flight values were obtained using the cross correlation between the source and the received signals. For the case of the FBP-AA image, the amplitude decay method was employed (Li *et al.*, 2008a). The values used to perform the backward projection in this case were calculated as the amplitude at the central frequency in the power spectrum of the recorded time-domain signals relative to water. The inverse radon transform with spline interpolation and Ram-Lak filter with a Hann window was employed to perform the FBP reconstruction in both cases (Kak and Slaney, 2001).

F. Algorithm overview

The complete reconstruction process is performed according to the scheme shown in Fig. 3. First, the data are split randomly into the desired number of subsets. The pressure field p generated by each emitter of the subset with the starting values of SS and AA is then computed using k-Wave [which solves Eq. (2)] and recorded in all the pixels of the computational grid. Next, the adjoint source is computed employing the time-reversed difference between the simulated and measured pressure field at each receiver's position. Using the adjoint source term, the adjoint field p^* is
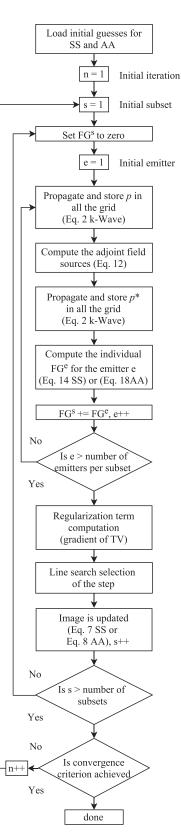

FIG. 3. Flow chart of the reconstruction algorithm used to update the SS and AA distributions.

then computed and recorded in all the pixels in the grid, again using k-Wave. After that, the contribution to the functional gradient for this projection is calculated (denoted FG^e in Fig. 3). This process is repeated for all the emitters included in the subset to obtain an estimate of the functional

gradient for the subset (denoted FG^s in Fig. 3). As the TV term that enters in the functional gradient [Eqs. (14) and (18)] is common to all the emitters of the subset, this is computed at the end of the subset. Next, the line-search algorithm is run and after the step size is obtained, the acoustic distribution is updated according to Eq. (7) for the SS and Eq. (8) for the AA. To complete a full-iteration, the same process is repeated for all subsets. Finally, a convergence criterion (discussed in Sec. IV A) is evaluated. If it is not fulfilled, the updated distribution is used as the starting value for the next iteration. The whole process is repeated until the convergence criterion is satisfied.

IV. NUMERICAL EXPERIMENTS

A. Overview of the numerical experiments

In order to test the performance of the proposed algorithm, simulated data from two numerical phantoms were generated using typical values of SS and AA in water and several constituents of the breast tissue (Szabo, 2004; Duck, 1990). The numerical experiments were performed in 2D to reduce computation times. The USCT geometry was a ring array of radius 54 mm with $N = 200$ uniformly distributed transducers. This circular configuration is employed in several prototypes of USCT scanner for breast cancer detection (Duric et al., 2009; Li et al., 2008b; André et al., 2013; Medina-Valdés et al., 2015) and ensures a constant spatial resolution and good angular coverage. The simulations were conducted on a $128\,\text{mm} \times 128\,\text{mm}$ grid represented by 256×256 grid points with a 20 grid point perfectly matched layer positioned outside the domain (Treeby and Cox, 2010a). The simulations to obtain the reference data were performed sequentially from emitter 1 to 200 using all 200 receivers for each transmitter. The pressure field at the detector positions in Cartesian space was calculated from the pressure at the grid points at each time step via linear interpolation. The transmitted signal was a Gaussian enveloped three-cycle sinusoidal tone burst with a 1 MHz central frequency. The signals were sampled for 854 time points with a time step of 100 ns. The simulation time for each projection for a single emitter was 0.43 s using an Intel (Santa Clara, CA) Core i7-3930K CPU (central processing unit) at 3.20 GHz with an NVIDIA GeForce GTX 780 GPU.

Each image update was performed using the functional gradient estimated from 4 emitters, i.e., the total data were divided into 50 subsets. Based on initial tests, this number of subsets provides a significant improvement in the total reconstruction time ($\sim50\times$ with respect to the use of one subset, i.e., using all the data in each image update), without introducing artifacts in the reconstruction. One full-iteration, using the signals from all 200 emitters, consists of 50 image updates. The convergence criterion employed was the slope of a line fitted to the norm of the global error as a function of the image updates. The reconstructions were stopped when the slope for an entire iteration (in this case 50 images updates) was less than 0.1.
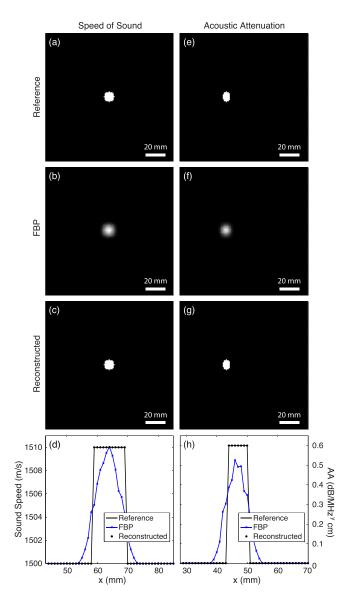

FIG. 4. (Color online) Reconstruction of a noiseless ideal case. (a) Reference SS map. (b) Initial SS map reconstructed using FBP. (c) Reconstructed SS map. (d) Profiles through the SS maps for the reference, FBP initial guess, and reconstructed image at the line $y = 64\,\text{mm}$. (e) Reference AA map. (f) Initial AA map reconstructed using FBP. (g) Reconstructed AA map. (h) Profiles through the AA maps for the reference, FBP initial guess, and reconstructed image at the line $y = 64\,\text{mm}$.

B. Reconstruction of an ideal case

First, a simple numerical phantom consisting of a homogenous map of water covering the whole field-of-view with two centered spots with either a change in SS or AA was investigated (Fig. 4). In this example, the image was reconstructed from noiseless data, and no regularization was employed. This allows the limits of the reconstruction method to be evaluated. The SS distribution was reconstructed using a FBP reconstruction for the initial SS distribution. The FBP-SS image is shown in Fig. 4(b) and was obtained in 0.3 s. As the goal of this ideal case was to test the limits of the algorithms, the actual map of AA was employed when updating the SS distribution. Similarly, the AA distribution was reconstructed using the actual map of the SS (although in this case the SS is reconstructed

J. Acoust. Soc. Am. **141** (3), March 2017

Pérez-Liva et al.   1601

perfectly), and a FBP reconstruction for the initial AA distribution. The FBP-AA image is shown in Fig. 4(f) and was also obtained in 0.3 s. The results of the reconstruction of the SS and AA maps are shown in Figs. 4(c) and 4(g). One-dimensional profiles across the reconstructions are shown in Figs. 4(d) and 4(h). In this ideal case, the method is able to achieve a perfect recovery of the margins and values of both the SS and AA distributions. This demonstrates the capability of the algorithm to obtain the correct solution for both distributions in the absence of noise and when the alternate acoustic distribution is available (i.e., the AA to recover the SS and vice versa). It also demonstrates the advantages of the FWI formulation over ray-tracing algorithms. The reconstruction of each acoustical property in this example was obtained in 27 min using two iterations.

C. Reconstruction of a realistic simulated breast phantom

A numerical phantom with several structures simulating breast tissue was also investigated (see Figs. 5 and 6). After the forward simulation, random Gaussian noise was added to the recorded data to give a signal-to-noise ratio (SNR) of 50 dB. This is similar to the SNR achievable with our experimental USCT prototype (Medina-Valdés *et al.*, 2015; Perez-Liva *et al.*, 2015). Due to the presence of noise in the data, the TV-based edge-preserving regularization explained in Sec. II B was employed in the reconstructions. In this case, the parameters μ and θ [see Eqs. (5) and (6)] were set to $\mu = 9 \times 10^{-6}$ and $\theta = 0.2$ for the SS regularization, and $\mu = 1 \times 10^{-8}$ and $\theta = 0.2$ for the AA regularization. These values gave adequate artifact control without significantly

FIG. 6. (Color online) Reconstruction of the AA for a breast phantom. (a) Reference AA map. (b) Initial AA map reconstructed using FBP. (c) Reconstructed AA map using the converged SS map. (d) Profiles through the AA maps for the reference, FBP initial guess, and reconstructed image at the line $y = 53$ mm (shown with the white dashed line).

compromising the image quality. The reconstructed SS and AA maps were obtained with two iterations (27 min). Even though these reconstruction times are reasonable, this could be further reduced in the future by using alternative optimization schemes, such as the quasi-Newton method (Snyman, 2005).

To quantify the quality of the reconstructions, the mean and standard deviation of the pixel values within several regions of interest (ROIs) located inside the lesions and structures of the numerical phantom were obtained and compared with the expected values in those ROIs (Table I). The noise level (ratio of the standard deviation and mean value inside the ROIs) and bias (difference between expected and mean values) of the reconstructed images were also calculated for each ROI. Furthermore, profiles across the reconstructed distributions were taken to obtain the resolution of the reconstructed images. This was estimated as the distance required for the edge response to rise from 10% to 90% (Li *et al.*, 2014). Resolution was calculated at the phantom-water interface.

As can be seen in Fig. 5(c), the SS distribution can be recovered with high accuracy. The bias between the reconstructed and expected values is below 0.5% for all ROIs. Moreover, the regularization employed in the reconstruction algorithm significantly reduces the effect of noise. The noise level is below 0.9% for all ROIs and the edges of the different structures are preserved. The resolution was estimated to be ∼1 mm, which is close to the wavelength at the central frequency of the signals.

In comparison, the reconstructed AA distribution is more sensitive to noise and strongly dependent on any errors
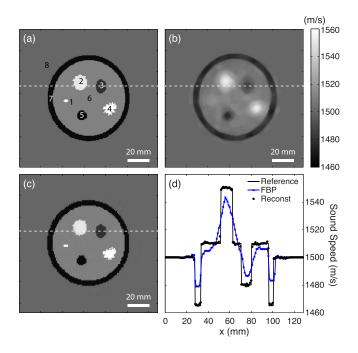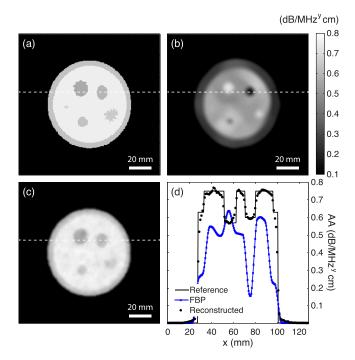

FIG. 5. (Color online) Reconstruction of the SS for a breast phantom. (a) Reference SS map. The numbers correspond to regions of interest (ROIs) given in Table I. (b) Initial SS map reconstructed using FBP. (c) Reconstructed SS map. (d) Profiles through the SS maps for the reference, FBP initial guess, and reconstructed image at the line $y = 53$ mm (shown with the white dashed line).

TABLE I. Mean values, standard deviation, noise, expected values, and bias at the ROIs shown in Fig. 5(a) for the SS and the AA distributions.

	ROI number	Mean value (m/s)	Standard deviation	Noise (%)	Expected value (m/s)	Bias (%)
SS	1	1481.47	4.43	0.30	1480	0.10
	2	1555.56	11.25	0.72	1560	0.28
	3	1467.30	7.72	0.53	1470	0.18
	4	1561.97	14.00	0.90	1570	0.51
	5	1548.41	6.07	0.39	1550	0.10
	6	1510.19	0.68	0.05	1510	0.01
	7	1467.01	6.82	0.46	1470	0.20
	8	1499.90	0.24	0.02	1500	0.01
		[dB/(MHz^y cm)]			[dB/(MHz^y cm)]	
AA	1	0.626	0.028	4.47	0.60	4.33
	2	0.674	0.022	3.26	0.65	3.69
	3	0.657	0.025	3.81	0.63	4.29
	4	0.724	0.003	0.41	0.68	6.47
	5	0.591	0.035	5.92	0.57	3.68
	6	0.756	0.011	1.46	0.75	0.80
	7	0.565	0.103	18.23	0.63	10.32
	8	0.005	0.001	20.00	0.0022	127.27

methods is also similar (Pratt *et al.*, 2007; Li *et al.*, 2014; Sandhu *et al.*, 2016) and the reconstruction is, as reported here, dependent on the errors in the reconstructed SS distribution. Therefore, noisy distributions are obtained as a result for the AA with both methods. One distinct advantage of the time domain formulation presented here is that it avoids having to select the right set of frequencies to be inverted and the appropriate number of iterations to perform at each frequency. This seems to be a key requirement of the frequency domain formulation needed to mitigate the ripples encountered in the reconstructed distributions (Li *et al.*, 2014; Sandhu *et al.*, 2016).

V. SUMMARY AND CONCLUSIONS

In this work, a time domain full-wave inversion algorithm for the reconstruction of both the SS and AA distributions in USCT is proposed. The algorithm is based on an adjoint formulation derived from the fractional Laplacian wave equation, and allows both distributions to be efficiently reconstructed within a common framework. The efficacy of the algorithm is demonstrated with two numerical examples. In the ideal case of noiseless data and given the exact distribution of the alternate material parameter (i.e., AA to recover SS, and SS to recover AA), both the AA and SS distributions can be reconstructed perfectly. In the more general case using a realistic geometry, Gaussian noise added to the reference signals, and a FBP reconstruction for the initial estimations, the proposed algorithm is capable of recovering accurately the shape and values of the structures in the image. Compared to ray-tracing algorithms, the results obtained demonstrate significant improvements in resolution and accuracy. Moreover, comparison of the resolution and noise of the reconstructed images with previous studies based on frequency domain algorithms supports the equivalence of both formulations. However, the time domain formulation presented here avoids the need to select the appropriate set of frequencies, a step required by the frequency domain formulations. The main limitation is the high dependence of the AA reconstruction on any errors present in the reconstructed SS and the noise in the signals. In future, it would be useful to explore other possible ways to define the misfit function to mitigate this. While the convergence rates for the current study are reasonable, the use of other optimization schemes might also increase the rate of convergence. The application of this method for the reconstruction of real data, and the extension to three dimensions (3D) will be explored as part of future work.

present in the reconstructed SS distribution. There are two main contributions to noise. First, errors in the SS map will affect the trajectory of the propagating waves and, consequently, the attenuation experienced between the source and emitter pairs. Second, for the misfit function given in Eq. (5), the differences between simulated and observed signals due to AA are much smaller than the differences due to time misalignments coming from changes in the SS, i.e., the selected cost function is much more sensitive to variations in SS than in AA (Tejero *et al.*, 2015). This may be an important limitation when noise is comparable to the differences between simulated and observed signals due to attenuation, as in this case the adjoint source will be dominated by noise. This highlights the fact the AA estimate is very sensitive to the SNR in the data and the accuracy of the reconstructed SS map.

In this example, the maximum noise level in the reconstructed AA map was 18% and the bias between simulated and expected values in the selected ROIs was typically below 10%. The exception is within water (ROI 8) where higher bias was observed. This is due to the very small attenuation coefficient in water, and the large difference in the AA values with respect to the other soft tissues. A possible improvement of the methods would be to identify the water region from the SS map, and use this to constrain the reconstruction of AA. The estimated resolution in the reconstructed AA map was ∼6 mm.

For reference, these results can be compared to the performance of using a frequency domain formulation of the adjoint field to obtain the functional gradients for the SS and the AA. For example, in Li *et al.* (2014), both the SS and AA distributions were investigated using a numerical phantom and noiseless data. For the SS, similar resolution can be obtained using both formulations (on the order of the acoustic wavelength). For the AA case, the performance of both

André, M., Wiskin, J., and Borup, D. (**2013**). "Clinical results with ultrasound computed tomography of the breast," in *Quantitative Ultrasound in Soft Tissues, Part IV: Ultrasound Computer Tomography*, edited by J. Mamou and M. L. Oelze (Springer, New York), Chap. 15, pp. 395–432.

Anis, F., Lou, Y., Conjusteau, A., Su, R., Oruganti, T., Ermilov, S. A., Oraevsky, A. A., and Anastasio, M. A. (**2014**). "Investigation of the adjoint-state method for ultrasound computed tomography: A numerical and experimental study," Proc. SPIE **8943**, 894337.

Boyd, N. F., Martin, L. J., Bronskill, M., Yaffe, M. J., Duric, N., and Minkin, S. (**2010**). "Breast tissue composition and susceptibility to breast cancer," J. Natl. Cancer Inst. **102**(16), 1224–1237.

Chen, W., and Holm, S. (**2004**). "Fractional Laplacian time-space models for linear and nonlinear lossy media exhibiting arbitrary frequency power-law dependency," J. Acoust. Soc. Am. **115**, 1424–1430.

Devaney, A. (**1981**). "Inverse-scattering theory within the Rytov approximation," Opt. Lett. **6**, 374–376.

Devaney, A. (**1982**). "Inversion formula for inverse scattering within the Born approximation," Opt. Lett. **7**, 111–112.

Duck, F. (**1990**). "Acoustic properties of tissue at ultrasonic frequencies," in *Physical Properties of Tissue: A Comprehensive Reference Book* (Harcourt Brace Jovanovich, London), Chap. 4, pp. 73–135.

Duric, N., Li, C., Littrup, P., Glide-Hurst, C., Huang, L., Lupinacci, J., Schmidt, S., Rama, O., Bey-Knight, L., and Xu, Y. (**2008**). "Multi-modal breast imaging with ultrasound tomography," Proc. SPIE **6920**, 69200O.

Duric, N., Littrup, P., Li, C., Rama, O., Bey-Knight, L., Schmidt, S., and Lupinacci, J. (**2009**). "Detection and characterization of breast masses with ultrasound tomography: Clinical results," Proc. SPIE **7265**, 72651G.

Duric, N., Littrup, P., Li, C., Roy, O., Schmidt, S., Seamans, J., Wallen, A., and Bey-Knight, L. (**2015**). "Whole breast tissue characterization with ultrasound tomography," Proc. SPIE **9419**, 94190G.

Fornage, B. D., Lorigan, J. G., and Andry, E. (**1989**). "Fibroadenoma of the breast: Sonographic appearance," Radiology **172**, 671–675.

Hudson, H. M., and Larkin, R. S. (**1994**). "Accelerated image reconstruction using ordered subsets of projection data," IEEE Trans. Med. Imaging **13**, 601–609.

Jackson, D. D. (**1972**). "Interpretation of inaccurate, insufficient and inconsistent data," Geophys. J. Int. **28**, 97–109.

Johnson, S. A., Abbott, T., Bell, R., Berggren, M., Borup, D., Robinson, D., Wiskin, J., Olsen, S., and Hanover, B. (**2007**). "Non-invasive breast tissue characterization using ultrasound speed and attenuation," in *Acoustical Imaging*, edited by André M. P. (Springer, Dordrecht, The Netherlands), pp. 147–154.

Kak, A. C., and Slaney, M. (**2001**). *Principles of Computerized Tomographic Imaging* (Society for Industrial and Applied Mathematics, Philadelphia), pp. 1–323.

Kretzek, E., Hopp, T., and Ruiter, N. (**2015**). "GPU-based 3D SAFT reconstruction including attenuation correction," Proc. SPIE **9419**, 94190E.

Li, C., Duric, N., and Huang, L. (**2008a**). "Comparison of ultrasound attenuation tomography methods for breast imaging," Proc. SPIE **6920**, 692015.

Li, C., Duric, N., and Huang, L. (**2008b**). "Breast imaging using transmission ultrasound: Reconstructing tissue parameters of sound speed and attenuation," in *IEEE International Conference on BioMedical Engineering and Informatics*, edited by Y. Peng and Y. Zhang (China), pp. 708–712.

Li, C., Duric, N., Littrup, P., and Huang, L. (**2009**). "*In vivo* breast sound-speed imaging with ultrasound tomography," Ultrasound Med. Biol. **35**, 1615–1628.

Li, C., Sandhu, G. S., Roy, O., Duric, N., Allada, V., and Schmidt, S. (**2014**). "Toward a practical ultrasound waveform tomography algorithm for improving breast imaging," Proc. SPIE **9040**, 90401P.

Lin, F., Nachman, A. I., and Waag, R. C. (**2000**). "Quantitative imaging using a time-domain eigenfunction method," J. Acoust. Soc. Am. **108**, 899–912.

Mast, T. D. (**1999**). "Wideband quantitative ultrasonic imaging by time-domain diffraction tomography," J. Acoust. Soc. Am. **106**, 3061–3071.

Mast, T. D. (**2000**). "Empirical relationships between acoustic parameters in human soft tissues," Acoust. Res. Lett. Online **1**, 37–42.

Medina-Valdés, L., Pérez-Liva, M., Camacho, J., Udías, J., Herraiz, J., and González-Salido, N. (**2015**). "Multi-modal ultrasound imaging for breast cancer detection," Phys. Procedia **63**, 134–140.

Niesen, U., Shah, D., and Wornell, G. W. (**2009**). "Adaptive alternating minimization algorithms," IEEE Trans. Inform. Theory **55**, 1423–1429.

Norton, S. J. (**1999**). "Iterative inverse scattering algorithms: Methods of computing Frechet derivatives," J. Acoust. Soc. Am. **106**, 2653–2660.

Perez-Liva, M., Herraiz, J., Medina-Valdés, L., Camacho, J., Fritsch, C., Ibáñez, P., and Udías, J. (**2015**). "PD-0137: Ultrasound computed tomography for early breast cancer detection," in *Proceedings of 3rd ESTRO Forum 2015, published in Radiotherapy and Oncology*, (115), p. S65.

Peyré, G. (**2009**). "The numerical tours of signal processing," Comput. Sci. Eng. **13**(4), 94–97.

Pratt, R. G., Huang, L., Duric, N., and Littrup, P. (**2007**). "Sound-speed and attenuation imaging of breast tissue using waveform tomography of transmission ultrasound data," Proc. SPIE **6510**, 65104S.

Roy, O., Jovanović, I., Hormati, A., Parhizkar, R., and Vetterli, M. (**2010**). "Sound speed estimation using wave-based ultrasound tomography: Theory and GPU implementation," Proc. SPIE **7629**, 76290J.

Rudin, L. I., Osher, S., and Fatemi, E. (**1992**). "Nonlinear total variation based noise removal algorithms," Physica D **60**, 259–268.

Ruiter, N. V., Zapf, M., Hopp, T., Dapp, R., and Gemmeke, H. (**2012**). "Phantom image results of an optimized full 3D USCT," Proc. SPIE **8320**, 832005.

Sandhu, G. Y. S., Li, C., Roy, O., West, E., Montgomery, K., Boone, M., and Duric, N. (**2016**). "Frequency-domain ultrasound waveform tomography breast attenuation imaging," Proc. SPIE **9790**, 97900C.

Simonetti, F., Huang, L., Duric, N., and Littrup, P. (**2009**). "Diffraction and coherence in breast ultrasound tomography: A study with a toroidal array," Med. Phys. **36**, 2955–2965.

Snyman, J. (**2005**). *Practical Mathematical Optimization: An Introduction to Basic Optimization Theory and Classical and New Gradient-Based Algorithms* (Springer Science and Business Media, New York), Vol. 97, pp. 1–257.

Song, Z., Williamson, P. R., and Pratt, R. G. (**1995**). "Frequency-domain acoustic-wave modeling and inversion of crosshole data: Part II—Inversion method, synthetic experiments and real-data results," Geophysics **60**, 796–809.

Szabo, T. L. (**2004**). *Diagnostic Ultrasound Imaging: Inside Out* (Elsevier Academic, London), pp. 1–535.

Tarantola, A. (**1987**). *Inverse Problem Theory: Methods for Data Fitting and Parameter Estimation* (Elsevier, Amsterdam), pp. 1–601.

Tejero, C. J., Dagnino, D., Sallarès, V., and Ranero, C. R. (**2015**). "Comparative study of objective functions to overcome noise and bandwidth limitations in full waveform inversion," Geophys. J. Int. **203**(1), 632–645.

Treeby, B. E., and Cox, B. T. (**2010a**). "*k*-Wave: MATLAB toolbox for the simulation and reconstruction of photoacoustic wave fields," J. Biomed. Opt. **15**, 021314.

Treeby, B. E., and Cox, B. (**2010b**). "Modeling power law absorption and dispersion for acoustic propagation using the fractional Laplacian," J. Acoust. Soc. Am. **127**, 2741–2748.

Treeby, B. E., and Cox, B. (**2014**). "Modeling power law absorption and dispersion in viscoelastic solids using a split-field and the fractional Laplacian," J. Acoust. Soc. Am. **136**, 1499–1510.

Treeby, B. E., Jaros, J., Rendell, A. P., and Cox, B. (**2012**). "Modeling nonlinear ultrasound propagation in heterogeneous media with power law absorption using a *k*-space pseudospectral method," J. Acoust. Soc. Am. **131**, 4324–4336.

Wang, K., Matthews, T., Anis, F., Li, C., Duric, N., and Anastasio, M. (**2015**). "Waveform inversion with source encoding for breast sound speed reconstruction in ultrasound computed tomography," IEEE Trans. Ultrason. Ferroelectr. Freq. Control **62**, 475–493.

Wiskin, J., Borup, D., Johnson, S., Berggren, M., Abbott, T., and Hanover, R. (**2007**). "Full-wave, non-linear, inverse scattering," in *Acoustical Imaging*, edited by M. P. André (Springer, Dordrecht, The Netherlands), pp. 183–193.

Zhou, C., Cai, W., Luo, Y., Schuster, G. T., and Hassanzadeh, S. (**1995**). "Acoustic wave-equation traveltime and waveform inversion of crosshole seismic data," Geophysics **60**, 765–773.